

## Systematic Analyses of Proton Elastic Scattering between $65 < E_p < 200$ MeV with Microscopic Effective Interaction

Norio YAMAGUCHI, Sinobu NAGATA and Junji MICHİYAMA<sup>\*)</sup>

*Department of Applied Physics, Miyazaki University, Miyazaki 880*

(Received March 14, 1986)

Systematic analyses of proton elastic scattering from nuclei between the bombarding energies of  $65 < E_p < 200$  MeV were performed with use of the folding model potentials. The density- and incident energy-dependent effective interactions to be folded were evaluated microscopically under the Brueckner-Hartree-Fock approximation in nuclear matter. The experimental data of cross sections, analyzing powers and spin rotation functions could be reproduced satisfactorily. Especially the quality of fit was excellent for the data at  $E_p = 65$  MeV. It was shown that the medium effects still play important roles in this energy region. Dependence of the folding model potential on the effective interactions was also investigated. The Pauli- and starting energy-rearrangement potentials were found to reduce the net depth of the folding potential by more than 15%. Some problems in the folding procedure were also discussed.

### § 1. Introduction

During the past decade, experimental data of proton scattering from nuclei have become abundant, covering various target nuclei and a wide energy range.<sup>1)~6)</sup> We noticed that most of these recent experiments retain high accuracy and include measurements of not only the differential cross sections but also other physical factors such as analyzing powers and spin rotation functions. The increase of these data of high accuracy has helped to eliminate the ambiguity and to reveal new aspects of the potential model. For instance, experimental data with high momentum transfer will provide information on the internal shape of the optical model potential (OMP). It is quite interesting that some analyses of these data have indicated the failure of traditional Woods-Saxon potential shape.

The microscopic theory of OMP has been progressively developing<sup>7)~10)</sup> and it is now recognized that the nuclear matter approach within Brueckner-Hartree-Fock approximation (abbreviate as BHF approach) is successful and reliable in describing low energy scattering phenomena. In this approach the OMP of nuclear matter is approximated by the BHF term in the low density expansion for the mass operator. Then the OMP of finite nuclei is obtained with either of the following two approaches under the local density approximation (LDA). One is to replace it at each position by the OMP of nuclear matter for the same density. The other is to construct it by folding the complex reaction ( $G$ -) matrices calculated in nuclear matter into the density distribution of a target nucleus.

Within the latter method, we have proposed in Ref. 9) the complex effective interaction CEG (complex effective, Gaussian form factor) which is microscopically evaluated employing Hamada-Johnston (HJ) potential<sup>11)</sup> as the basic  $N$ - $N$  force. Using this CEG we have pointed out that the density and incident energy dependences of the effective interaction play a substantial role in improving the fit to the experimental data below 50 MeV of incident energy. These dependences are caused by the Pauli blocking effect and the binding effect associated with the propagation of nucleon in nuclear medium, which are

<sup>\*)</sup> Present address: Tokyo Research Laboratory, Matsushita Electronics Corporation, Kanagawa 214.

the so-called medium effects.

In this paper we extend our previous work<sup>9)</sup> to higher energies and investigate the reliability of the non-relativistic BHF approach with respect to the medium effects.

First, we attempt to clarify how the medium effects, which have been responsible for the saturation properties in nuclear bound state problems, appear in the nucleon-nucleus scattering phenomena in the energy region above 50 MeV.

As the incident energy increases up to about 200 MeV the medium effect through the Pauli blocking seems to be less important and that through the binding effect seems to disappear because the OMP becomes very weak in this energy region. However it is pointed out that the medium effects are still surviving around this energy region.<sup>12)</sup> We should note that the effect of the core singularity of the basic  $N$ - $N$  force will become more appreciable as the momentum transfer increases. It is just around this energy region that the real part of the one-body potential of nuclear matter changes its sign. This means that the magnitude of the folding model potential (FMP) is consequently rather small and hence depends on the effective interaction more sensitively. As an example the origin of non Woods-Saxon shape of FMP will be investigated.

Below the pion threshold energy, the realistic  $N$ - $N$  forces used in this paper are parametrized so that they can accurately describe the  $N$ - $N$  scattering phase shifts within the non-relativistic formalism. Therefore we use the non-relativistic framework throughout this paper for the analyses of the experimental data in the energy range of 65–200 MeV.

We also investigate the dependence of FMP on the effective interactions which reflect the properties of the basic  $N$ - $N$  forces such as the core singularity and the ratio of the strength of the tensor part to that of the central one ( $v_T/v_C$ ) in the triplet even ( $^3E$ ) state.

In the bound state and low energy scattering problems it has been shown<sup>9),13)</sup> that the latter property largely influences the attractive parts in the  $^3E$  state through the medium effects. Thus the resultant OMP's differ about 10% in the central depth of the real part between those calculated from HJ and OPEG<sup>14)</sup> potentials. In the high energy scattering problems, on the contrary, the core singularity of the basic  $N$ - $N$  force, which is closely related to the structure of the nucleons and the repulsive interaction caused by the heavy mesons exchange, might more appeal through high momentum transfer processes. The effect of the core singularity will be concentrated to the inner shape of FMP and then affect the backward angle cross sections.

Throughout this paper, we use newly evaluated CEG for the analyses of the experimental data at the energy region of  $65 < E_p < 200$  MeV. Also, we refer to other effective interactions, which are evaluated using Reid Soft Core<sup>15)</sup> (RSC) and OPEG potentials as the basic  $N$ - $N$  forces.

We discuss the rearrangement effects which are important higher-order-diagrams in the multiple scattering process. These effects have played important roles in reproducing the reasonable one-body potential in the nuclear bound state problem.<sup>16)</sup> It is suggested<sup>9),17),18)</sup> that the same situation also takes place in the scattering problems. These are considered to be other aspects of medium corrections to the FMP.

For the systematic analyses, we cover the target nuclei  $^{12}\text{C}$ ,  $^{16}\text{O}$ ,  $^{40}\text{Ca}$ ,  $^{90}\text{Zr}$  and  $^{208}\text{Pb}$ . These overall survey will help us in investigating the subjects mentioned above.

Section 2 outlines our formulation. Sections 3 and 4 are for the results and discussions respectively. Conclusions are given in § 5.

## § 2. Formulation

The effective interactions we use in the present calculation are those which have been obtained within the BHF approach in nuclear matter. The details to construct them have been reported in Ref. 9). Since the effects of higher partial waves are not negligible around the energy region which we are now interested in, we take into account all the partial waves of  $J \leq 5$  for HJ and OPEG cases. Other numerical conditions are the same as those in Ref. 9).

The convergence of the density expansion for the OMP is strongly related to the auxiliary potential for the particle state in the propagator of the  $G$ -matrix. However the optimal choice of the auxiliary potential has not yet been fully investigated. Here we employ the BHF potential, which is defined by the same equation as the OMP in our approach. We regard the auxiliary potential as being real, namely we assume the following condition is satisfied:

$$|V_{\infty}(k)| \equiv |\text{Re} \cdot U_{\infty}(k)| \gg |W_{\infty}(k)| \equiv |\text{Im} \cdot U_{\infty}(k)|, \quad (1)$$

where  $U_{\infty}$  is the OMP of nuclear matter. Self-consistency is checked through  $V_{\infty}(k)$  and finally the incident energy  $E$  is determined by the energy-momentum relation,

$$E(k) = \hbar^2 k^2 / 2m + V_{\infty}(k). \quad (2)$$

We solve the complex  $G$ -matrix equation with the intermediate momentum up to  $10k_F$  for  $k_F = 1.4$  and  $1.0 \text{ fm}^{-1}$ , and  $15k_F$  for  $k_F = 0.6 \text{ fm}^{-1}$ . By transforming the resultant  $G$ -matrices into the coordinate space, the effective interaction is numerically obtained. Then it is decomposed into central, spin-orbit and tensor components. Further the central components are averaged over the included angular momenta.

The RSC and OPEG base effective interactions are thus numerically stored. We construct CEG with three-range Gaussian form factors, whose parameters are determined by simulating the diagonal matrix elements of the one-body potential obtained from HJ. In the fitting procedure, to obtain reasonable core strength, we also refer to the radial form of the effective interaction based on the OPEG potential which has Gaussian cores.

The functional form of CEG is expressed as

$$^{\text{eff}}G(r; k_F, E) = \sum_i^3 v_i^{ST}(k_F, E) e^{-(r/\lambda_i)^2}, \quad (3)$$

where

$$v_i^{ST}(k_F, E) = \sum_{j,k}^3 a_{ijk}^{ST} E^{j-1} k_F^{k-1}. \quad (4)$$

Tables I~III show the ranges and the parameters  $a_{ijk}^{ST}$  of Eqs. (3) and (4) for the energy range of  $65 < E < 200 \text{ MeV}$ .\*) The parameters for the energy below  $50 \text{ MeV}$  have already been reported in Ref. 9).

The folding potential is now commonly used and the technique to evaluate it is well

\*) Since we employ a quadratic function to simulate the  $k_F$ -dependence, present CEG does not fall to free  $t$  matrices as the density decreases. We recommend to fix  $k_F$  as  $0.4$  for lower densities than  $k_F = 0.4$  and as  $1.8$  for higher densities than  $k_F = 1.8 \text{ fm}^{-1}$ .

Table I. Ranges and parameters  $a_{ij}^{\pi}$  of Eq. (4) for real central component of CEG ( $50 < E < 200$  MeV).

$i$	range	$j$	$k$	$S=0$ $T=0$	$S=0$ $T=1$	$S=1$ $T=0$	$S=1$ $T=1$
1	2.5000	1	1	0.87332E 01	-0.17637E 01	-0.12273E 01	0.66760E 00
			2	0.	-0.31048E 01	-0.55180E 01	0.
			3	0.	0.11172E 01	0.24300E 01	0.
		2	1	0.	-0.35811E-01	-0.71980E-01	-0.45000E-03
			2	0.	0.49786E-01	0.12405E 00	0.
			3	0.	-0.16842E-01	-0.48730E-01	0.
		3	1	0.	0.13451E-03	0.33439E-03	0.
			2	0.	-0.18000E-03	-0.52907E-03	0.
			3	0.	0.58730E-04	0.20124E-03	0.
2	0.8900	1	1	-0.14072E 03	-0.24094E 03	0.56542E 03	-0.17120E 03
			2	0.17254E 03	-0.44195E 03	-0.21731E 04	0.69035E 02
			3	0.61875E 00	0.21819E 03	0.10024E 04	-0.11694E 02
		2	1	0.21634E 01	-0.12162E 01	-0.10701E 02	0.29928E 00
			2	-0.18337E 01	0.62270E 01	0.27339E 02	-0.43279E 00
			3	0.50853E 00	-0.33598E 01	-0.13196E 02	0.16671E 00
		3	1	-0.41296E-02	0.46362E-02	0.34380E-01	0.31700E-03
			2	0.44704E-02	-0.21748E-01	-0.87788E-01	0.43065E-04
			3	-0.12221E-02	0.12040E-01	0.43640E-01	-0.14713E-03
3	0.5000	1	1	0.49275E 03	0.91134E 03	-0.14497E 04	0.87139E 03
			2	-0.20533E 03	0.13550E 04	0.59605E 04	-0.20363E 03
			3	0.59156E 02	-0.64094E 03	-0.26447E 04	0.88688E 02
		2	1	-0.28012E 01	0.43589E 01	0.32181E 02	-0.45145E 00
			2	0.13993E 01	-0.22088E 02	-0.81426E 02	0.20198E 00
			3	-0.15406E 00	0.11872E 02	0.38943E 02	-0.12191E 00
		3	1	0.49995E-02	-0.19441E-01	-0.10833E 00	-0.26473E-02
			2	-0.25829E-02	0.79743E-01	0.27353E 00	0.27709E-02
			3	-0.30400E-03	-0.43039E-01	-0.13392E 00	-0.56909E-03

established. Here we denote some points which are especially incorporated in our calculation.

Present microscopic FMP  $U_F(R) = V_F(R) + iW_F(R)$  is obtained in the case of CEG with use of a calculational method given in Ref. 19), in which the Gaussian expansion of the density and the pseudopotential for the exchange term are used.

In the case of finite nuclei with  $N \neq Z$ , where the proton Fermi momentum is  $k_F^p$  and neutron  $k_F^n$ , we use the different momentum  $k_F^p$  and  $(k_F^p + k_F^n)/2$  for the density parameters in the effective interactions for proton-proton and proton-neutron cases, respectively. As to the energy parameter  $E$ , the Coulomb energy  $V_C$  is subtracted from the incident energy  $E_{in}$  at each position of the projectile proton, i.e., an effective energy  $E_{in} - V_C$  is used for  $E$ . We should note that the energy dependence of FMP is caused partly by the energy dependence of the interaction and partly by the exchange term through the local momentum  $k$ .

Since we use a local expression for the optical potential, to take into account the effect of the non-locality in the real potential, the imaginary part of the FMP should be multiplied<sup>20)</sup> by the effective  $k$ -mass  $m_k/m$ , which results in an equivalent mean free path for the propagation of a nucleon specified by the energy-momentum relation of Eq. (2) with

Table II. Ranges and parameters  $a_{ijk}^{ST}$  of Eq. (4) for imaginary central component of CEG ( $50 < E < 200$  MeV).

$i$	range	$j$	$k$	$S=0 \quad T=0$	$S=0 \quad T=1$	$S=1 \quad T=0$	$S=1 \quad T=1$
1	2.5000	1	1	$-0.13414E \ 00$	$-0.68250E \ 00$	$0.82834E \ 00$	$-0.14179E \ 00$
			2	$-0.38035E \ 00$	$0.42500E \ 00$	$-0.27688E \ 01$	$-0.29758E \ 00$
			3	$0.32639E \ 00$	$-0.62500E -01$	$0.14476E \ 01$	$0.23059E \ 00$
		2	1	$-0.71960E -02$	0.	$-0.35630E -01$	$-0.11037E -01$
			2	$0.10006E -01$	0.	$0.58641E -01$	$0.11279E -01$
			3	$-0.67416E -02$	0.	$-0.24495E -01$	$-0.37709E -02$
		3	1	$0.16608E -04$	0.	$0.11619E -03$	$0.55741E -04$
			2	$-0.42289E -04$	0.	$-0.19685E -03$	$-0.53230E -04$
			3	$0.27681E -04$	0.	$0.82098E -04$	$0.14847E -04$
2	0.8900	1	1	$-0.22994E \ 01$	$-0.52543E \ 03$	$-0.30873E \ 04$	$0.23067E \ 02$
			2	$-0.36040E \ 01$	$0.59294E \ 03$	$0.46661E \ 04$	$-0.40841E \ 02$
			3	$0.24294E \ 01$	$-0.17290E \ 03$	$-0.18033E \ 04$	$0.18022E \ 02$
		2	1	$-0.15605E \ 00$	$0.40527E \ 01$	$0.32094E \ 02$	$-0.69592E \ 00$
			2	$0.91000E -01$	$-0.57165E \ 01$	$-0.54218E \ 02$	$0.68063E \ 00$
			3	$-0.51375E -01$	$0.18672E \ 01$	$0.21887E \ 02$	$-0.23909E \ 00$
		3	1	$-0.44886E -04$	$-0.83867E -02$	$-0.92993E -01$	$0.11770E -02$
			2	$-0.37845E -03$	$0.14229E -01$	$0.16011E \ 00$	$-0.19687E -02$
			3	$0.20266E -03$	$-0.48873E -02$	$-0.65372E -01$	$0.91253E -03$
3	0.5000	1	1	$-0.69644E \ 01$	$0.15076E \ 04$	$0.12935E \ 05$	$-0.56148E \ 02$
			2	$-0.11345E \ 02$	$-0.15591E \ 04$	$-0.20820E \ 05$	$0.10671E \ 03$
			3	$0.38094E \ 01$	$0.40978E \ 03$	$0.84369E \ 04$	$-0.47640E \ 02$
		2	1	$-0.96409E \ 00$	$-0.85571E \ 01$	$-0.13913E \ 03$	$0.20108E \ 01$
			2	$0.24025E -01$	$0.11050E \ 02$	$0.24336E \ 03$	$-0.21313E \ 01$
			3	$-0.28688E -01$	$-0.29957E \ 01$	$-0.10168E \ 03$	$0.66281E \ 00$
		3	1	0.	$0.90762E -02$	$0.40660E \ 00$	$-0.52605E -02$
			2	0.	$-0.16853E -01$	$-0.72284E \ 00$	$0.71320E -02$
			3	0.	$0.33930E -02$	$0.30466E \ 00$	$-0.27355E -02$

Table III. Ranges and parameters  $a_{ijk}^{ST}$  of Eq. (4) for spin-orbit component of CEG ( $50 < E < 200$  MeV).

$i$	real					imaginary			
	range	$j$	$k$	$S=1 \quad T=0$	$S=1 \quad T=1$	range	$j$	$k$	$S=1 \quad T=1$
1	0.6742	1	1	$-0.34590E \ 03$	$-0.51880E \ 03$	1.8257	1	1	$0.63466E \ 00$
							2	1	$-0.19014E -02$
							3	1	$-0.53503E -05$
2	0.4394	1	1	$0.92365E \ 03$	$0.63700E \ 03$	0.5872	1	1	$-0.22216E \ 02$
							2	1	$-0.80243E \ 00$
							3	1	$0.25754E -02$
3						0.4472	1	1	$0.21089E \ 02$
							2	1	$0.33663E \ 01$
							3	1	$-0.49799E -02$

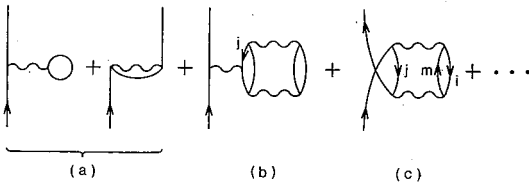


Fig. 1. Some leading terms in the low density expansion for the optical potential. The wavy line represents the renormalized interaction of the ladder correlation.

use of  $U_\infty$  in place of  $V_\infty$ . The effective  $k$ -mass is given as

$$\frac{m_k}{m} = \left(1 + \frac{m}{k} \frac{\partial V_\infty(k)}{\partial k}\right)^{-1}. \quad (5)$$

As to the spin-orbit potential, we follow the folding method in Ref. 21) in which the finite range effect is taken into account by including the higher multipoles.

In almost all works reported so far, the OMP of nuclear matter is identified to

be the lowest order in the low density expansion of mass operator. It corresponds to diagram (a) in Fig. 1. Diagram (b) shows the starting energy ( $\omega$ -) rearrangement and diagram (c) is the Pauli-rearrangement. These effects on proton scattering were investigated in Refs. 9) and 17) for the elastic and in Ref. 18) for the inelastic cases, respectively. Contributions from both of diagrams (b) and (c) reduce the depth of OMP. Although we can estimate the net effects of both of these rearrangement terms by  $\partial G/\partial \rho$ , we investigate the respective effect separately. The  $\omega$ -rearrangement effect can be estimated by the equation

$$(b) = - \sum_{|k_j| < k_F} \chi_j \langle \mathbf{k} \mathbf{k}_j | G | \mathbf{k} \mathbf{k}_j \rangle^{\text{AS}} = - \bar{\chi}(k_F) \cdot U_\infty(k), \quad (6)$$

the superscript AS means antisymmetrization. In Eq. (6) we approximate the wound integral  $\chi_j$  by an averaged value  $\bar{\chi}(k_F)$  obtained in our previous calculation for the bound state problem.<sup>22)</sup> The Pauli-rearrangement is given by

$$(c) = - \sum_{|k_i|, |k_j| < k_F} \sum_{|k_m| > k_F} \langle \mathbf{k}_i \mathbf{k}_j | G | \mathbf{k}_m \mathbf{k} \rangle \frac{1}{E_i + E_j - E_m - E} \langle \mathbf{k}_m \mathbf{k} | G | \mathbf{k}_i \mathbf{k}_j \rangle^{\text{AS}}. \quad (7)$$

We can estimate the contribution from this diagram by using CEG as a substitute of  $G$ . By assuming that the incident momentum is sufficiently higher than the Fermi momentum and thus the momenta and energies for the occupied states are zero, Eq. (7) leads to

$$(c) \sim \left(\frac{2k_F^3}{3\pi^2}\right)^2 \frac{1}{2E} \frac{3}{8} \{ |{}^{\text{eff}}G(k; {}^3S)|^2 + |{}^{\text{eff}}G(k; {}^1S)|^2 \}, \quad (8)$$

where  ${}^{\text{eff}}G(k)$  is the matrix elements for a transfer momentum  $k$ .

### § 3. Results

In the following calculation we use, unless specified, the RGM density<sup>23)</sup> for  ${}^{12}\text{C}$  and HF densities<sup>24)</sup> for  ${}^{16}\text{O}$ ,  ${}^{40}\text{Ca}$ ,  ${}^{90}\text{Zr}$  and  ${}^{208}\text{Pb}$ , respectively.

We first analyze the experimental data<sup>4), 25)</sup> obtained at RCNP for the incident energy  $E_p = 65$  MeV. These data were analyzed<sup>4)</sup> initially with the traditional Woods-Saxon potential restricting to forward angle data. Those potential searches are almost satisfactory in reproducing the data. However to compensate for a lack of the information on the inner shape of the potential, a revised potential family was model-independently examined<sup>25)</sup> including the backward angle data together with newly obtained spin-

rotation-function data. This potential should be understood as an “experimental OMP”. Figure 2 shows the real and imaginary central potentials for  $^{40}\text{Ca}$  target. In this figure solid lines show the present results obtained by the folding of CEG. By comparing these with dashed lines and long dashed lines, which mean the orthodox Woods-Saxon<sup>4)</sup> and the model-independent potentials<sup>25)</sup> respectively, it is quite encouraging that our real FMP shown in the upper half of Fig. 2 comes close to the model-independent potential over all regions. As to the imaginary FMP shown in the lower half of Fig. 2, we find that our potential is similar to the Woods-Saxon potential and shallower in the internal region than the model-independent one.

Figures 3~5 show the calculated cross sections, analyzing powers and spin-rotation-functions  $Q$  for the cases of  $^{40}\text{Ca}$ ,  $^{90}\text{Zr}$  and  $^{208}\text{Pb}$  targets. These figures indicate that the fit to the data is quite satisfactory in consideration that the present approach is completely without free parameters. Especially it is to be stressed that the fit of  $Q$ -parameters in Fig. 5 is excellent at least in the forward angle region. It is noted that the fit to the data is better for heavier target where LDA works well. Of course the fit is improved by multiplying factor  $N$  to the potential, as shown in Fig. 6 for the case of  $^{90}\text{Zr}$  target. These factors,  $N_{\text{real}}=0.95$  and  $N_{\text{imaginary}}=0.80$ , can be used to estimate the reliability of the present approach. However we notice that these free parameters are rather restricted in the sense that they do not change the radial form factor of the potential. In addition, our major concern is rather to clarify the reach of the present approach. Thus, we do not

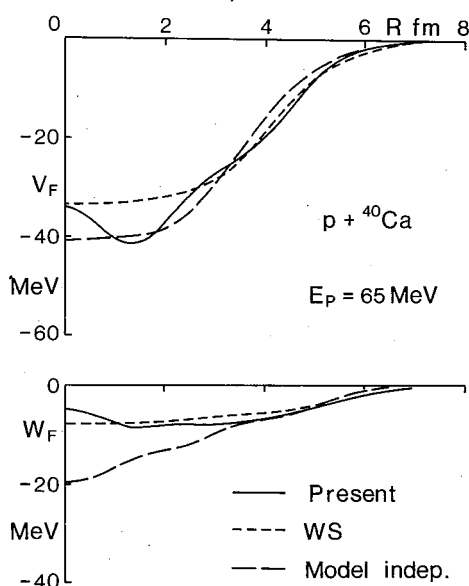


Fig. 2. Central potential for  $p + ^{40}\text{Ca}$  at  $E_p = 65$  MeV. Woods-Saxon (WS) potential is taken from Ref. 4) and model independent potential is taken from Ref. 25).

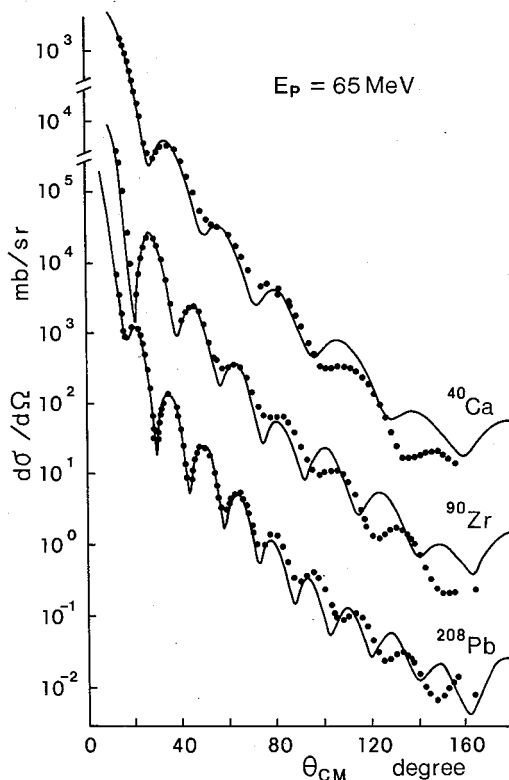


Fig. 3. Differential cross sections for  $p + ^{40}\text{Ca}$ ,  $^{90}\text{Zr}$  and  $^{208}\text{Pb}$  at  $E_p = 65$  MeV.

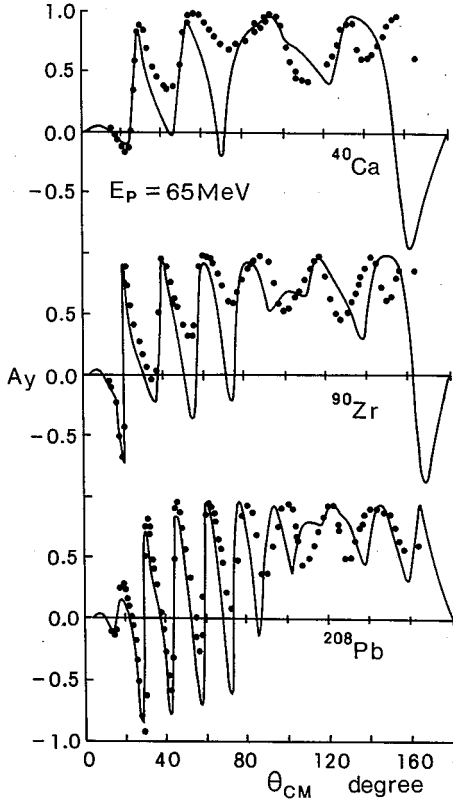


Fig. 4. Analyzing powers for  $p + {}^{40}\text{Ca}$ ,  ${}^{90}\text{Zr}$  and  ${}^{208}\text{Pb}$  at  $E_p = 65$  MeV.

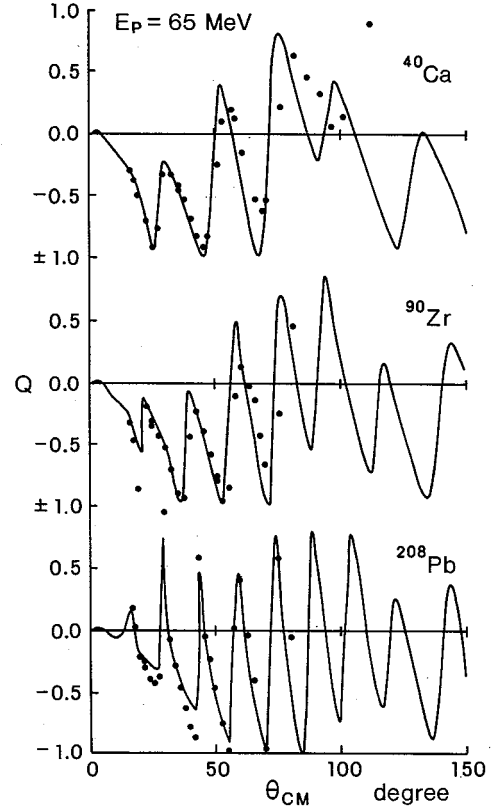


Fig. 5. Spin-rotation-functions for  $p + {}^{40}\text{Ca}$ ,  ${}^{90}\text{Zr}$  and  ${}^{208}\text{Pb}$  at  $E_p = 65$  MeV.

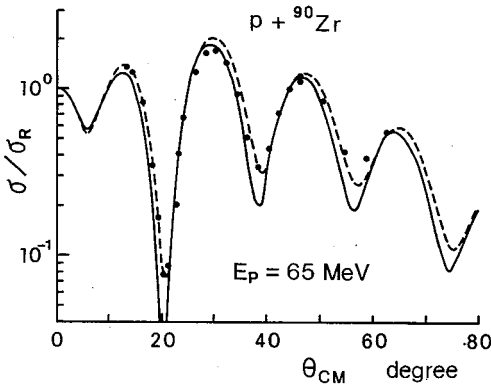


Fig. 6. Differential cross sections divided by the Rutherford cross sections for  $p + {}^{90}\text{Zr}$  at  $E_p = 65$  MeV. Solid line shows the present result while in dashed line we multiply the factors 0.95 and 0.80 to the real and imaginary central potentials respectively.

analyses with the non-relativistic BHF approach have been performed by several authors.<sup>26),27)</sup> Our potential shape of the real central FMP shown in Fig. 7 is fairly different from those in Fig. 2 in Ref. 26) and Fig. 1 in Ref. 27). It may seem curious that the present real

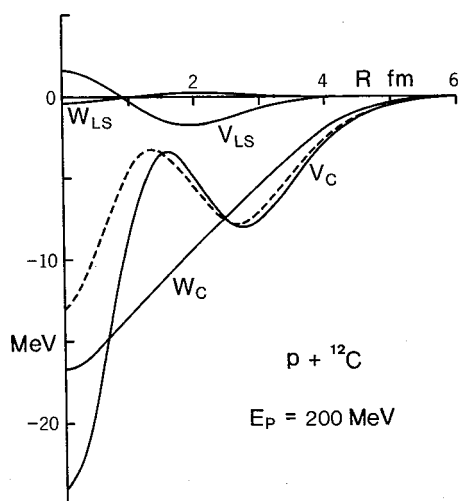
introduce these adjustable parameters in the following calculations. Table IV shows the volume integral and mean square radius of the real central FMP in comparison with the results in Refs. 4) and 25). It is noteworthy that the present microscopic approach can reproduce the systematicity of these bulk properties without artificial adjustment.

Next we analyze the data at an energy region between 100–200 MeV. We first show the calculated FMP for the case of  ${}^{12}\text{C}$  target at  $E_p = 200$  MeV in Fig. 7 where a typical wine-bottle-bottom shape is formed. Aside from the analyses with the standard Woods-Saxon or double Woods-Saxon potential,<sup>5)</sup> the microscopic



Table IV. Volume integral and mean square radius of the real central potential at  $E_p=65$  MeV.

		$^{16}\text{O}$	$^{40}\text{Ca}$	$^{48}\text{Ca}$	$^{90}\text{Zr}$	$^{208}\text{Pb}$
$J/A$ $\text{MeV}\cdot\text{fm}^3$	present	336	326	333	330	340
	Woods-Saxon <sup>4)</sup>	347	334	315	319	331
	Model-indep. <sup>25)</sup>		316–333			
$\langle r^2 \rangle$ $\text{fm}^2$	present	11.52	16.17	17.83	23.43	36.57
	Woods-Saxon <sup>4)</sup>	12.35	17.58	18.39	25.35	39.18

Fig. 7. FMP's by CEG interaction for  $p+^{12}\text{C}$  at  $E_p=200$  MeV.

ter model<sup>23)</sup> is realistic in describing the structure of  $^{12}\text{C}$ , we proceed our analyses with solid lines in Fig. 7.

Figure 8 shows the calculated cross sections. Experimental data are taken from Refs. 5) and 28). The results appear to be satisfactory considering that the LDA is less applicable to light nuclei. We next show in Fig. 9 the results for  $^{16}\text{O}$  target. Experimental data are taken from Refs. 6) and 29). As to the 135 MeV data it is reported that the standard Woods-Saxon potential works well.<sup>29)</sup> On the contrary, a double Woods-Saxon potential, in other words the wine-bottle-bottom shaped potential, is needed<sup>6)</sup> to explain the 200 MeV data. This finding indicates that the wine-bottle-bottom shape is gradually formed as the energy increases. A mechanism of the wine-bottle-bottom shape formation will be discussed in § 4. Figure 10 shows the analyzing powers and the spin-rotation-functions for the cases of  $^{12}\text{C}$  and  $^{16}\text{O}$  targets at  $E_p=200$  MeV. Experimental data are taken from Ref. 30). In the case of  $^{16}\text{O}$ , the positive experimental values of  $Q$  at around  $\theta_{\text{CM}}=40^\circ$  seem to discriminate the two models, DWS(+) and DWS(-) in the analyses in Ref. 6), which have different behaviour at the innermost part of the potential, and our FMP well reproduces the behaviour of DWS(-) potential and the experimental results<sup>30)</sup> over the region of  $\theta_{\text{CM}}=40^\circ$ .

Figure 11 shows the cross sections for  $^{208}\text{Pb}$  target. Experimental data are taken from Ref. 1). We notice that the fit of the solid line is not very good but the fall-off pattern is reproduced on the whole over a wide momentum-transfer region. The fit to the

central FMP differs considerably from that in Ref. 26) even though both of them start from the same HJ potential. The reason for this difference is as follows. First the used density distribution is different from each other and this gives the different steepness to the FMP at the innermost region ( $R < 1$  fm). The difference near the wine-bottle-bottom region ( $1 < R < 3$  fm) may be attributed to our assumption of Gaussian function for the core part of the effective interaction, which results in a more attractive potential. If we take the density of double Woods-Saxon type,<sup>5)</sup> the resultant FMP becomes moderate only in the innermost region and this is shown with the dashed line in Fig. 7. However, since we consider that the three-alpha cluster model<sup>23)</sup> is realistic in describing the structure of  $^{12}\text{C}$ , we proceed our analyses with solid lines in Fig. 7.

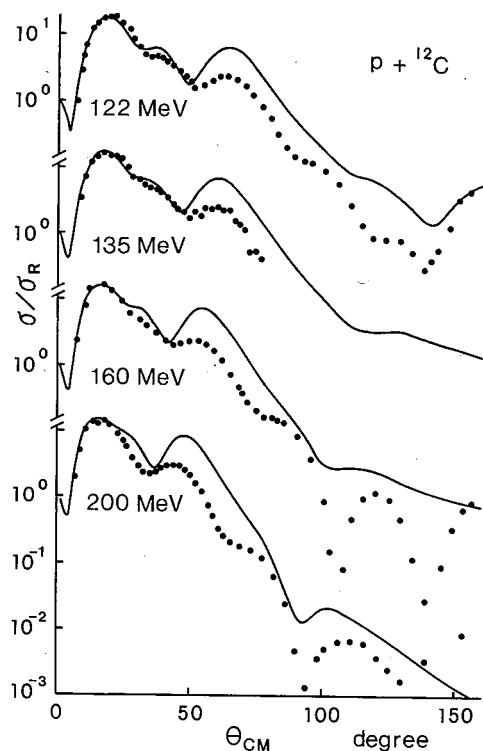


Fig. 8. Differential cross sections divided by the Rutherford cross sections for  $p + {}^{12}\text{C}$ .

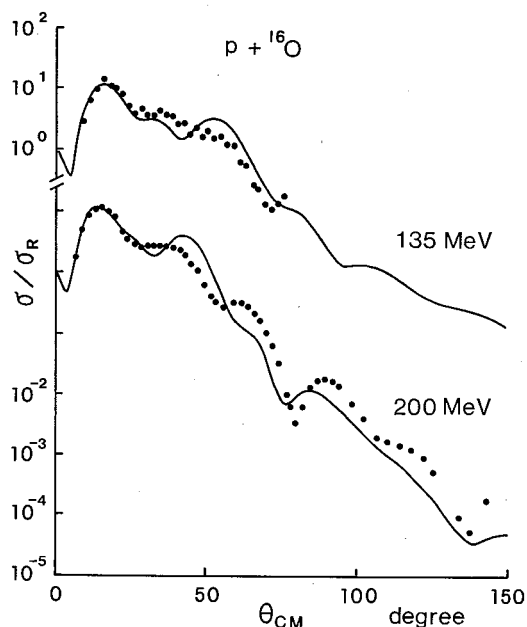


Fig. 9. Differential cross sections divided by the Rutherford cross sections for  $p + {}^{16}\text{O}$ .

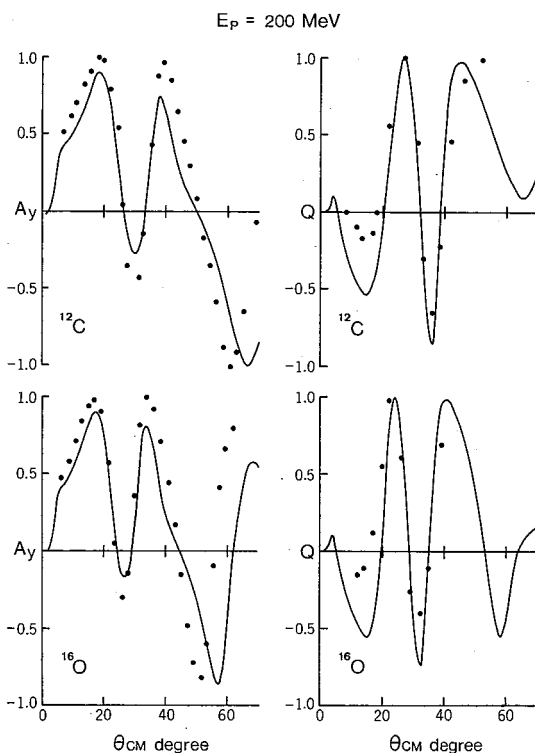


Fig. 10. Analyzing powers ( $A_y$ ) and spin-rotation functions ( $Q$ ) for  $p + {}^{12}\text{C}$  and  ${}^{16}\text{O}$  at  $E_p = 200$  MeV.

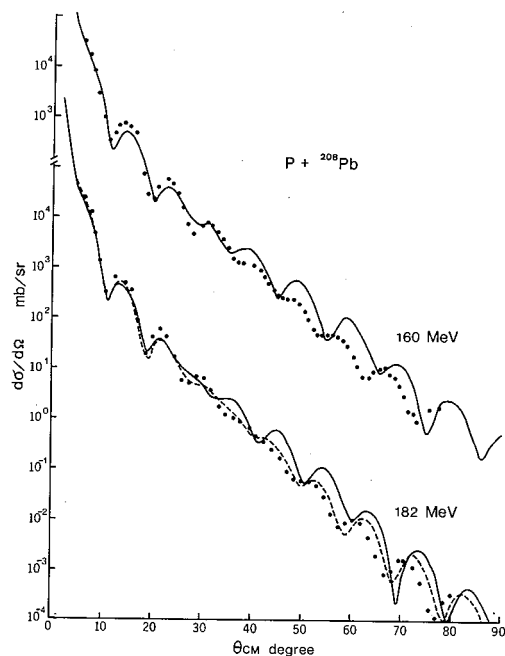


Fig. 11. Differential cross sections for  $p + {}^{208}\text{Pb}$ . The solid lines denote the results with HF density and the dashed one with the 3-parameter Gaussian density.

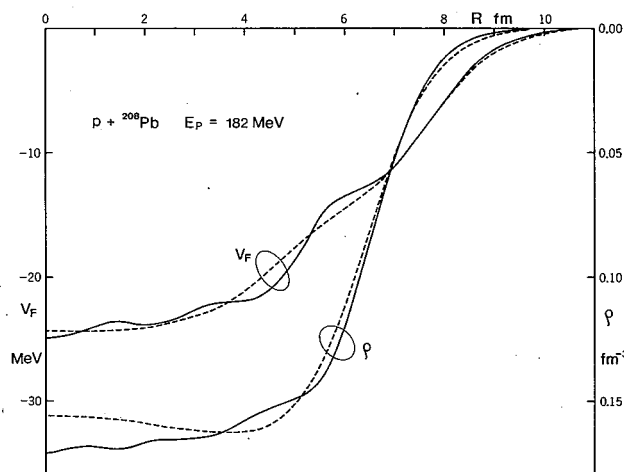


Fig. 12. Sensitivity of the FMP to the target density distribution. The solid lines denote the HF density and the resultant FMP. The dashed lines are those by the 3-parameter Gaussian density.

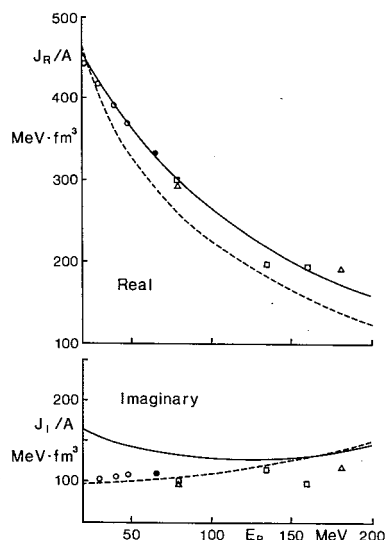


Fig. 13. Energy dependence of the volume integrals of the real and imaginary central FMP for  $p + {}^{40}\text{Ca}$ . Solid curves are the present results and dashed curves are by Dirac-Hartree approach in Ref. 32). Dots are taken from Ref. 4), open circles are from Ref. 31), squares are from Ref. 1) and triangles are taken from Ref. 2).

data of the analyzing powers has a similar quality to those cases of  ${}^{12}\text{C}$  and  ${}^{16}\text{O}$  in Fig. 10. Here we refer to the excellent fit reported by Hamburg group<sup>21)</sup> with the use of the effective interaction based upon the Paris potential. We find that their quality of fit is due mainly to their choice of the smooth density distribution. We show in Fig. 12 the dependence of the FMP with CEG on the used density distributions. In this figure, the solid line is obtained with HF density and the dashed line is the one obtained with the three parameter Gaussian-density-distribution used in Ref. 21). If we apply the latter FMP and neglect, following Ref. 21), the non-locality correction to the imaginary central potential, we can attain the same quality of fit as that in Ref. 21). This is shown with the dashed line in Fig. 11 for the case  $E_p = 182$  MeV. From this result the present CEG is considered to have a similar character to the Hamburg interaction around this energy region. However we encounter an excessively large reaction-cross-section in this case.

The above results show that the FMP's and resultant differential cross sections are affected appreciably by the used density distribution through the density-dependence of the effective interaction.

As a next step, we investigate the systematicity of the FMP in its bulk properties. Figure 13 shows the energy dependence of the volume integral of the central FMP for the case of  ${}^{40}\text{Ca}$  target. As to the real part  $J_R/A$ , it is very striking that the present FMP can realize the systematicity extracted from several different approaches.<sup>1),2),4),31)</sup> We notice that present FMP's give larger values than those of Dirac-Hartree approach<sup>32)</sup> of  $\sigma$ - $\omega$  model. This is because, in a high energy region, the latter approach tends to make the inner potential shallower than that with the present non-relativistic BHF approach through the cancellation between the scalar and vector potentials.

As to the imaginary part  $J_I/A$ , our results are somewhat larger than the

phenomenological ones at lower energies. As discussed in Ref. 9), this may be attributed to the fact that we employed the continuum level for the low-excited particle states in solving the  $G$ -matrix equation in nuclear matter. Thus, the present  $J_1/A$  yields reasonable values as the energy increases, where  $W_\infty$  is less sensitive to the choice of the low excited spectra. In some experiments the reaction cross sections are measured and we can estimate the favourable magnitude of  $J_1/A$  by comparing the calculated reaction cross sections with them. For the cases of  $p+^{12}\text{C}$  at  $E_p=200$  MeV and  $p+^{208}\text{Pb}$  at  $E_p=182$  MeV, our results are 240 and 1764 mb respectively and these are very close to the experimental values of 218<sup>33)</sup> (at  $E_p=231$  MeV) and 1767<sup>33)</sup> (at  $E_p=226$  MeV)mb.

#### § 4. Discussion

In this section we discuss the results in § 3 and related properties of FMP.

##### 4.1. Medium effect

It has been confirmed in the bound state and low energy scattering problems that the density- and starting (or incident) energy-dependences of the effective interaction in nuclear medium play essential roles in explaining the experimental data. It is interesting to investigate how these medium effects appear in high energy scattering problems. As an example we show in Fig. 14 the effect of the density-dependence of the effective interaction to the FMP. In this figure the FMP's are obtained numerically with use of RSC base effective interaction. The inclusion of density-dependence is shown with the

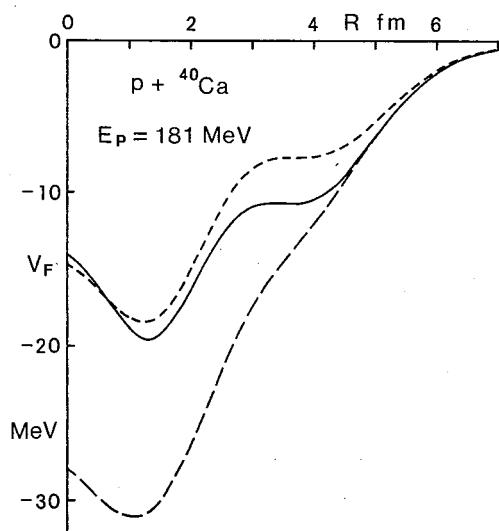


Fig. 14. Effects of the density-dependence of RSC base numerical effective interaction on the FMP. Solid line shows the inclusion of density-dependence. In long dashed and dashed lines the densities are fixed at  $k_F=0.6$  and  $1.4 \text{ fm}^{-1}$  respectively.

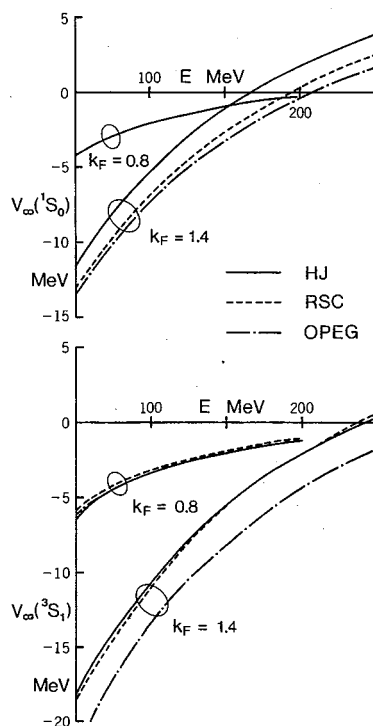


Fig. 15. Contributions of the  $S$  states in  $N-N$  forces to the one-body potential  $V_\omega(E(k); k_F)$  in nuclear matter.

solid line, while in the long-dashed and dashed lines the parameter  $k_F$  is fixed at 0.6 and  $1.4\text{fm}^{-1}$  respectively. This figure clearly shows the importance of the density-dependence still in this energy region.

It is well known that the effective interactions are strongly dependent on the used basic  $N$ - $N$  forces through the medium effects. To see this, we compare in Fig. 15 the contributions of the  $S$  state to the OMP of nuclear matter. We first notice that the  $N$ - $N$  force dependence of the OMP is present even at the higher energy region as the density increases. As to the  $^1S_0$  state shown in the upper half of Fig. 15, the differences come from the different singular nature of the short range core of the  $N$ - $N$  forces. We notice that the result with HJ, from which the present CEG is constructed, is about 1~2 MeV less attractive and crosses zero towards repulsive at a 20~40 MeV lower energy in the region of 200 MeV in comparison with those obtained with the soft core potentials. As to the  $^3S_1$  state shown in the lower half of Fig. 15, the difference between RSC and OPEG potentials, both of which have soft cores, are attributed to the different  $v_T/v_C$  ratio. The above tendency in the  $N$ - $N$  force dependence is consistent with those discussed in Refs. 13) and 34). The contributions from higher partial waves are not negligible around this energy region. However we find that the above situation still holds. As discussed above, the OMP of nuclear matter is changed depending on which  $N$ - $N$  force we use. This property should cause the differences in density-dependence of the effective interaction. Then the subsequent FMP becomes also  $N$ - $N$  force dependent at higher densities.

Since this medium effect is strong enough as shown in Fig. 14, the shape of FMP is affected by the density functions of the target nucleus. This effect is more appreciable at the region around where the density fluctuates. Such an example was shown in Fig. 12 for the case of  $^{208}\text{Pb}$ . In the present BHF approach, we speculate that the HF density is appropriate in the sense that we can describe the bound state and scattering problem within the same framework. In this case, the neutron densities are given under the same reliability as the proton densities.

Apart from the above problems, the shape of FMP is also affected by the following factors. One of them is the functional form used for expressing the core part of the effective interaction as denoted in § 3 for the case of  $^{12}\text{C}$ . Another is the treatment of the exchange potential. In the folding procedure we introduced a pseudopotential, as mentioned in § 2, to take into account the knock-on exchange process. This pseudopotential is constructed to reproduce the exchange contribution in nuclear matter. It has a finite range form factor<sup>19)</sup> and is equivalent to an improved LDA potential in Ref. 7). The present exchange contribution coincides with that obtained by the local WKB approximation<sup>35)</sup> in the case of the uniform density distribution. In the case of finite nuclei, our treatment reduces the inner part of FMP by about several percent and makes the tail longer in comparison with the local WKB approximation.

Together with the discussions in § 3, we conclude that the net change in the shape of FMP is about 10% depending on the above factors. Among them we find that the shape of FMP is predominantly affected by the radial form of the density distribution of the target nucleus.

#### 4.2. Wine-bottle-bottom shape

In this subsection we discuss the formation of wine-bottle-bottom shape and the relation to the characteristics of the effective interactions. Within the non-relativistic

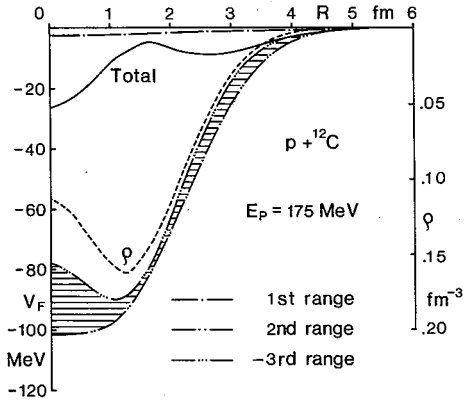


Fig. 16. Decomposition of the FMP to the contributions from each range of CEG.

region and the second range (two-dots-dashed line) corresponding to the strong attractive region. Since the range of core part is short, folding of it leads to the radial form which roughly follows that of the density distribution of the target nucleus (dashed line). On the contrary the second range of the interaction is longer and the resulting potential is expected to be more diffuse. Then we find that, in the high density region, both contributions almost cancel each other and, in the tail region, this cancellation becomes moderate. Thus the difference between respective contributions, the shaded area in Fig. 16, forms a wine-bottle-bottom shape. Here it is meaningful to point out that the extent of the cancellation at the highest density is sensitive to the core strength of the effective interaction as discussed in § 3 and that some parts of the shaded area are due to the medium effects. The density-dependence arguments the attractive part of the effective interaction at lower densities and then the diffuseness of the contribution from the second range is enhanced. In other words the density-dependence of the effective interaction determines the extent of wine-bottle-bottom shape. As a result, 1) the wine-bottle-bottom shape appears near  $E=150$  MeV depending on the growth of the core effect through the cancellation between the short range repulsive part and the long range attractive part, and 2) the extent of its steepness depends on the interaction through its density-dependence, i.e., the medium effect.

In this respect, we comment on a wine-bottle-bottom shape which appears in the FMP constructed in the Dirac-Hartree theory. In almost all of their works the medium effect is not included in the interaction and so the shape is formed only by the cancellation between the short range repulsive part by the vector meson and the long range attractive part by the scalar meson. Thus the wine-bottle-bottom shape is less prominent because of its no density-dependence. However, at higher energies it is natural to employ the relativistic framework, thus we expect that a consistent description based upon the relativistic BHF approach<sup>37)</sup> will be in practical use.

#### 4.3. Higher order correction

Medium effects are not limited only to the ladder correlation. They are also derived from the higher order diagrams in the density expansion of the mass operator. On the basis of successful hole-line expansion in the binding energy problem, we here discuss the effects of  $\omega$ - and Pauli-rearrangement diagrams. As described in Ref. 9) the  $\omega$ -

BHF approach there are some arguments<sup>26),27),36)</sup> about the origin of the wine-bottle-bottom shape. In Fig. 16 we divide the FMP into the contributions from each range of CEG for the case of  $p+^{12}\text{C}$  at  $E_p=175$  MeV. We notice that the contribution of the first range (dot-dashed line) is very small. This is because the outer part of the effective interaction is dominated by the OPEP tail which is cancelled out for the isospin saturated nuclei. Our concern lies in the difference between the contributions from the third range (three-dots-dashed line) which bears the repulsive core

rearrangement effect is repulsive and its density dependence can be approximated by a quadratic function of  $k_F$ .<sup>22)</sup> The inclusion of this diagram into the FMP reduces the inner part by more than 10%. The  $\omega$ -rearrangement effect reduces not only the real part but also the imaginary part of FMP by about 10% regardless of the incident energy (see Eq. (6)). Further we calculate the effect of Pauli-rearrangement to the FMP via Eq. (8) using CEG. We notice in Eq. (8) that the strength of the Pauli-rearrangement effect is proportional to  $\rho^2$  and then the real potential is reduced only in the interior region. For instance, around  $E_p=200$  MeV, this effect reduces the potential depth by about 4 MeV in the inner part ( $k_F=1.4$  fm<sup>-1</sup>) and by about 0.02 MeV in the outer part ( $k_F=0.6$  fm<sup>-1</sup>). These values are about 20% and 1% of the potential depths in the case of <sup>208</sup>Pb. Thus the effect of Pauli-rearrangement is comparable to the  $\omega$ -rearrangement effect in the interior region. The differential cross sections are then affected at the backward angles.

It has been shown in the bound state problem that the choice of the auxiliary potential  $U(k > k_F)=0$  in the propagator of the  $G$ -matrix equation is better for the convergence of the hole-line expansion series. Therefore, it seems also reasonable in the scattering problem to choose as  $U(k > k_F)=0$  or as  $U(k > k_F) \neq 0$  but with a gap at  $k_F$ , in order to reduce the higher order contributions.<sup>7)</sup> If we take such a potential, the  $G$ -matrix becomes less attractive and the FMP will be made shallow. Apart from this convergence problem, in usual treatments the auxiliary potentials are defined as being the same as the real part of the self-consistent OMP. When the imaginary part is far smaller than the real one, this treatment results in the cancellation of the diagrams for the one-body potential insertion in higher orders. In the high energy region, however,  $W_\infty$  is actually very large in comparison with  $V_\infty$  and so this cancellation in higher orders is not complete. It should be examined how the higher order diagrams contribute to the OMP and what choice of the auxiliary potential is best for the convergence.

Considering the above problems, we speculate that the present results with CEG, which includes only the lowest order contribution, would be changed by the inclusion of higher order corrections.

## § 5. Conclusions

We performed the systematic analyses of proton elastic scattering data below 200 MeV of incident energy from the microscopic viewpoint of the BHF approach. Our conclusions are as follows:

- (I) The present BHF approach for the OMP can follow the basic pattern of the experimental data of differential cross sections, analyzing powers and spin-rotation-functions. Especially the fit is excellent for the data at  $E_p=65$  MeV. In the reproduction of the data over a wide energy and mass number region, the medium effects, which are Pauli blocking and binding effects, still play important roles in this energy region.
- (II) The FMP is dependent on the used basic  $N$ - $N$  force, different off-shell properties of which result in a different character of the effective interaction through the medium effects.
- (III) Around an energy region of about 200 MeV, the wine-bottle-bottom shape is formed in the FMP. The origin is attributed to the cancellation between contributions of short range repulsive core and long range attractive part and further to the density-dependence of the effective interaction.

(IV) The shape of FMP's are sensitive to the density distribution of the target nucleus. The different treatment of the non-local exchange potential also causes the deviation to the shape of FMP. Uncertainties resulting from these folding procedures are found to be about 10%.

(V) The effects of  $\omega$ - and Pauli-rearrangement correlations in nuclear medium should be taken into account. These correlations reduce the depth of the real potential by roughly 15 to 20% in a inner region and change the results obtained with the effective interactions which simulate only the ladder correlation. Other higher order effects should also be investigated.

### Acknowledgements

The authors wish to express their appreciation to Professor T. Sakuda for his advice, encouragement and interest throughout the course of this work. They are indebted to Professor H. Sakaguchi for providing the data obtained at RCNP and giving many helpful advices. Sincere thanks are also expressed to Dr. M. Kamimura for his stimulating discussions and giving the chance to use the code of Gaussian expansion method.

This work was partly supported by the project on "Microscopic Optical Model Potential" organized by RCNP. The numerical computations were carried out at the Computer Centers of Kyushu and Miyazaki Universities.

### References

- 1) A. Nadasen et al., Phys. Rev. **C23** (1981), 1023.
- 2) P. Schwandt et al., Phys. Rev. **C26** (1982), 55.
- 3) L. G. Arnold, B. C. Clark, R. L. Mercer and P. Schwandt, Phys. Rev. **C23** (1981), 1949.
- 4) H. Sakaguchi et al., Phys. Rev. **C26** (1982), 944.
- 5) H. O. Meyer, P. Schwandt, W. W. Jacobs and J. R. Hall, Phys. Rev. **C27** (1983), 459.
- 6) G. W. Glover et al., Phys. Rev. **C31** (1985), 1.
- 7) J. Hufner and C. Mahaux, Ann. of Phys. **73** (1972), 525.  
J. P. Jeukenne, A. Lejeune and C. Mahaux, Phys. Rev. **C10** (1974), 1391; **C16** (1977), 80; Phys. Rep. **C25** (1976), 83.
- 8) F. A. Brieva and J. R. Rook, Nucl. Phys. **A291** (1977), 299, 317; **A297** (1978), 206; **A307** (1978), 493.
- 9) N. Yamaguchi, S. Nagata and T. Matsuda, Prog. Theor. Phys. **70** (1983), 459.
- 10) H. V. von Geramb, L. Rikus and K. Nakano, in *Proc. RCNP Int. Sympo. on Light Ion Reaction Mechanism*, Osaka, Japan, 1983, p. 78.
- 11) T. Hamada and I. D. Johnston, Nucl. Phys. **34** (1962), 382.
- 12) J. Kelly et al., Phys. Rev. Lett. **45** (1980), 2012.
- 13) Y. Akaishi and S. Nagata, Prog. Theor. Phys. Extra Number (1968), 476.
- 14) R. Tamagaki, Prog. Theor. Phys. **39** (1968), 91.
- 15) R. V. Reid, Ann. of Phys. **50** (1968), 411.
- 16) M. Kohno, S. Nagata and N. Yamaguchi, Prog. Theor. Phys. Suppl. No. 65 (1979), 200.
- 17) M. Kohno and D. W. L. Sprung, Nucl. Phys. **A397** (1983), 1.
- 18) T. Cheon, K. Takayanagi and K. Yazaki, Nucl. Phys. **A437** (1985), 301.
- 19) S. Nagata, M. Kamimura and N. Yamaguchi, Prog. Theor. Phys. **73** (1985), 512.
- 20) J. W. Negele and K. Yazaki, Phys. Rev. Lett. **47** (1981), 71.  
S. Fantoni, B. L. Friman and V. R. Pandharipande, Phys. Lett. **104B** (1981), 89.
- 21) L. Rikus and H. V. von Geramb, Nucl. Phys. **A426** (1984), 496.
- 22) N. Yamaguchi, T. Kasahara, S. Nagata and Y. Akaishi, Prog. Theor. Phys. **62** (1979), 1018.
- 23) M. Kamimura, Nucl. Phys. **A351** (1981), 456.
- 24) J. W. Negele, Phys. Rev. **C1** (1970), 1260.
- 25) H. Sakaguchi et al., J. Phys. Soc. Jpn. Suppl. **55** (1986), 61 and private communication.
- 26) A. M. Kobos, W. Haider and J. R. Rook, Nucl. Phys. **A417** (1984), 256.
- 27) L. Rikus, K. Nakano and H. V. von Geramb, Nucl. Phys. **A414** (1984), 413.
- 28) W. Bauhoff et al., Nucl. Phys. **A410** (1983), 180.



- 29) K. Amos et al., Nucl. Phys. **A413** (1984), 255.
- 30) E. J. Stephenson et al., J. Phys. Soc. Jpn. Suppl. **55** (1986), 316.
- 31) E. Fabrici et al., Phys. Rev. **C21** (1980), 830.
- 32) L. G. Arnold et al., Phys. Rev. **C25** (1982), 936.
- 33) P. U. Renberg et al., Nucl. Phys. **A183** (1972), 81.
- 34) S. Nagata, H. Bando and Y. Akaishi, Prog. Theor. Phys. Suppl. No. 65 (1979), 10.
- 35) G. L. Thomas, B. C. Sinha and F. Duggan, Nucl. Phys. **A203** (1973), 305.
- 36) C. Mahaux, in *Common Problems in Low- and Medium-Energy Nuclear Physics*, ed. B. Castel et al. (Plenum Publ. Corp., 1979), p. 265.
- 37) M. R. Anastasio, L. S. Celenza, W. S. Pong and C. M. Shakin, Phys. Lett. **C100** (1983), 327.